# LinPrim: Linear Primitives for Differentiable Volumetric Rendering

NICOLAS VON LÜTZOW, Technical University of Munich, Germany MATTHIAS NIESSNER, Technical University of Munich, Germany



Fig. 1. We propose LinPrim, a new method that leverages linear primitives - octahedra and tetrahedra - for differentiable volumetric rendering in order to facilitate 3D scene reconstruction for novel view synthesis. To this end, we propose a differentiable rendering pipeline in conjunction with a real-time capable rasterizer tailored to such primitives, thus achieving interactive frame rates for novel-view rendering and showcasing the potential of explicit polyhedral primitives in modern NVS workflows.

Volumetric rendering has become central to modern novel view synthesis methods, which use differentiable rendering to optimize 3D scene representations directly from observed views. While many recent works build on NeRF [Mildenhall et al. 2022] or 3D Gaussians [Kerbl et al. 2023], we explore an alternative volumetric scene representation. More specifically, we introduce two new scene representations based on linear primitives—octahedra and tetrahedra-both of which define homogeneous volumes bounded by triangular faces. This formulation aligns naturally with standard mesh-based tools, minimizing overhead for downstream applications. To optimize these primitives, we present a differentiable rasterizer that runs efficiently on GPUs, allowing end-to-end gradient-based optimization while maintaining realtime rendering capabilities. Through experiments on real-world datasets, we demonstrate comparable performance to state-of-the-art volumetric methods while requiring fewer primitives to achieve similar reconstruction fidelity. Our findings provide insights into the geometry of volumetric rendering and suggest that adopting explicit polyhedra can expand the design space of scene representations.

CCS Concepts:  $\bullet$  Computing methodologies  $\rightarrow$  Rasterization; Machine learning approaches; Point-based models.

 ${\it Additional\ Key\ Words\ and\ Phrases:\ novel\ view\ synthesis,\ 3D\ reconstruction,\ scene\ representations}$ 

#### 1 Introduction

Novel View Synthesis (NVS) enables a holistic understanding of 3D scenes given only 2D observations. This capability is essential to a range of applications, including VR/AR, robotics, and autonomous

Authors' Contact Information: Nicolas von Lützow, nicolas.von-luetzow@tum.de, Technical University of Munich, Germany; Matthias Nießner, niessner@tum.de, Technical University of Munich, Germany.

driving. The success of state-of-the-art NVS approaches depends heavily on the chosen scene representations and the processes used to render them. In addition to visual quality, the representations have inherent characteristics that largely impact the ability to work with the reconstructed scenes in downstream applications. Explicit representations have proven particularly desirable due to their easily interpretable and manipulable structures.

Representations used in NVS approaches often differ from the triangle-mesh-based approaches used in most 3D pipelines. Triangle meshes, while universal in traditional 3D content creation, are challenging to optimize directly for NVS tasks. Consequently, exploring NVS representations that combine desirable properties of high visual fidelity, performance, stability, and integration into downstream applications is crucial. Although it is possible to convert between most common NVS and traditional representations, doing so adds complexity and usually degrades visual quality [Huang et al. 2024; Tang et al. 2023]. This limits the practicality of 3D reconstructions derived from images and consequently hinders their broader adoption.

The strongest visual quality in NVS applications is currently achieved by approaches relying on *Neural Radiance Fields* (NeRF) [Barron et al. 2021, 2022, 2023; Mildenhall et al. 2022]. Although the results are impressive, NeRFs encode an implicit function, making them suboptimal for downstream applications; furthermore, the corresponding volumetric rendering process is expensive and often infeasible for real-time settings. More recently, *3D Gaussian Splatting* (3DGS) [Kerbl et al. 2023] introduced a real-time capable, explicit representation that also achieves strong visual performance. The

3DGS representation consists of 3D Gaussian kernels, which are optimized on known views to adjust their position and features. As evidenced by the large body of derivative works relying on 3DGS [Chen et al. 2024b; Huang et al. 2024; Mai et al. 2024; Tang et al. 2024; Yu et al. 2024], the explicit nature of the representation simplifies integration into other pipelines and settings.

Motivated by the scientific curiosity of how simple, bounded primitives can be used to reconstruct high-fidelity real-world scenes, we explore an alternative to 3DGS by employing transparent polyhedra as our scene representation. Specifically, we introduce two novel scene representations based on octahedron and tetrahedron primitives. Each primitive is characterized by a compact set of features that describe its position, vertices, opacity, and view-dependent appearance. These primitives are bounded by triangular faces and of homogeneous density, which makes them well-suited for direct integration into established graphics workflows and provides an intuitive representation that can be easily understood and modified.

We build on the 3DGS pipeline to accommodate the new primitives. Our method first constructs polyhedra from a concise set of features in a fully differentiable manner. During rendering, we then rely on simple ray-triangle intersections to determine the opacity of each primitive and successively blend them. As a result, we can backpropagate image-space errors through the intersection calculations to distribute gradients onto the geometric features of each polyhedron. The optimization pipeline remains analogous to 3DGS, yet the bounded, triangular geometry of our primitives expands the applicability of differentiable rendering pipelines. Finally, we analyze the photometric reconstruction quality and performance of our approaches on real-world scenes. We are able to show comparable results while retaining real-time rendering speeds.

To sum up, our contributions are as follows:

- We introduce two novel scene representations based on transparent octahedron and tetrahedron primitives.
- We derive gradient-based optimization processes for the representations to adjust the primitives and population based on known views.
- We demonstrate that our differentiable, GPU-based rendering pipeline is real-time capable and produces high-fidelity scene reconstructions on real-world datasets.

# 2 Related Works

Volumetric Rendering of Radiance Fields. A major innovation in NVS has been the development of volumetric rendering approaches that represent scenes as continuous radiance fields. The seminal Neural Radiance Fields [Mildenhall et al. 2022] demonstrated how to learn a 5D function, mapping 3D coordinates and viewing directions to color and density, using a neural network. The rendering process used is differentiable, enabling the optimization of the representation given a known set of input views. Since its introduction, many subsequent works have improved on the initial approach.

In particular, *Mip-NeRF* [Barron et al. 2021, 2022] and *Zip-NeRF* [Barron et al. 2023] have drastically improved the visual quality by introducing multi-scale representations, anti-aliasing, and learned compression techniques. *Instant-NGP* [Müller et al. 2022] takes a different approach by accelerating both training and inference times

via a multiresolution hash-based encoding strategy, allowing near real-time reconstruction and rendering.

Despite these advancements, NeRF-based methods remain primarily implicit, often resulting in comparatively high rendering and optimization costs. Their implicit nature can limit usability in downstream tasks. Since geometry and appearance are learned as continuous fields, no explicit surface representation is available by default. Using NeRF-based representations in downstream applications thus relies on specialized approaches or expensive post-processing [Tang et al. 2023; Wang et al. 2023].

Differentiable Point-based Rendering. Point-based rendering has traditionally been seen as an alternative to mesh-based pipelines due to its simplicity in handling geometry and varying levels of surface detail [Gross and Pfister 2011; Zwicker et al. 2001]. More recently, differentiable point-based methods have emerged, enabling end-to-end optimization of both geometry and appearance from image supervision [Kopanas et al. 2021; Xu et al. 2022].

The seminal work of 3D Gaussian Splatting [Kerbl et al. 2023] replaces traditional point primitives with elliptical Gaussian kernels. By optimizing the position and shape of the kernels from known views, they can create an explicit 3D reconstruction from known views. Additionally, each Gaussian can be efficiently "splatted" onto the screen space, allowing for real-time rendering performance.

Building on the foundation of 3D Gaussian Splatting, *Mip-Splatting* [Yu et al. 2024] tackles aliasing by controlling the maximum frequency of the splats, effectively reducing flickering and dilation artifacts. This is achieved by filtering and scaling Gaussian primitives to better match the level of detail required at different viewing distances, preventing excessively sharp or overlapping splats.

Other works replace the Gaussian distributions with other primitives to achieve improved performance. *Beyond Gaussians* [Chen et al. 2024a], replaces Gaussian kernels with linear kernels to achieve sharper and more precise results in high-frequency regions. Compared to our work, however, the primitives remain elliptical and non-homogeneous in density. In contrast, *EVER* [Mai et al. 2024] uses homogeneous density ellipsoids to replace alpha-blending with an exact rendering process, which avoids popping artifacts. *3D Convex Splatting* [Held et al. 2024] employs 3D smooth convexes, completely detaching it from the Gaussian context. Their primitives offer improved flexibility and reconstruction quality.

Although these methods offer notable improvements, we instead aim to explore novel representations that rely on simple distinct primitives. While all of the above methods introduce novel primitives or rendering processes, they share the general optimization process using known views and differentiable rendering. As such, we aim to foster innovation by exploring foundational primitives to improve the general understanding of the scene representations used in NVS settings. For this, our work focuses on transparent polyhedra bounded by triangular faces, keeping compatibility with conventional geometry-processing tools while maintaining high fidelity and rendering speed.

#### 3 Method

# 3.1 Linear Rendering Primitives

We introduce two representations based primarily on polyhedron primitives. For each primitive, a set of features that can accurately describe its shape needs to be defined. In our case, these include geometric parameters, position, opacity, and color.

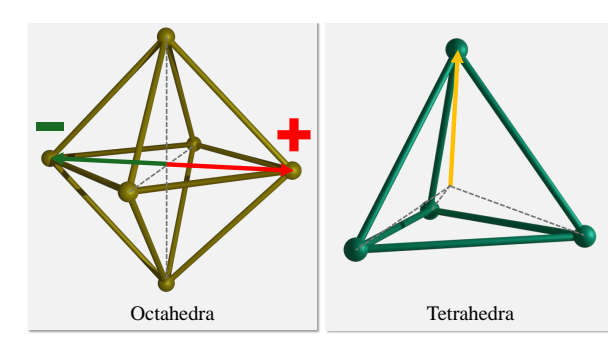


Fig. 2. Visualization of the distance features of each primitive type. For octahedra, vertices are always located on axes, with the distance being added in the wrong direction and subtracted in the other. For tetrahedra, no such symmetry exists; instead, each vertex has an individual distance value.

Octahedra. Importantly, there is a wide range of possible octahedra of which we only model a subset. We specifically ignore cases with non-triangular faces, which are difficult to handle and can lead to unpredictable numbers of vertices and edges. Moreover, to prevent degenerate cases, we limit the degrees of freedom by restricting vertex positions to lie on the coordinate axes relative to the center. To increase expressiveness, we instead optimize a rotation quaternion for each primitive, which ensures the shape can be oriented arbitrarily in space.

We enforce symmetry by choosing a single distance to describe opposing corners, as demonstrated in Fig. 2. Hence, each pair of opposite vertices shares the same distance from the center, effectively reducing the complexity of shape parameters. Aside from improving stability, this ensures that the center is always the true geometric center of the octahedron, simplifying downstream tasks such as bounding volume calculations and ray space approximation.

Tetrahedra. Although we focus primarily on octahedra, the same principles can be extended to accommodate many types of homogeneous volumes. As a particular example, we demonstrate the usage of tetrahedron primitives to reconstruct scenes. Contrary to octahedra, even regular tetrahedra are not symmetric along all axes and thus require adjustments to the stored features. In particular, we define four basis vectors, which describe directions from the center on which corners are located. All basis vectors are equally spaced such that they can represent regular tetrahedra. We then once again optimize for the distance between the center and each corner, as visualized in Fig. 2, keeping the process largely the same. Contrary to octahedra, this means that the optimized position can differ from the geometric center of the primitive.

Memory Requirements. In total, omitting color, each primitive is fully described by its center, rotation, corner distances, and opacity. For octahedra, this yields 11 floats in total, matching the parameter budget of a standard Gaussian kernel. Due to the absence of symmetry in our formulation, tetrahedra require 12 floats instead.

To describe colors and their view-dependent appearance, we utilize Spherical Harmonics (SH) coefficients, following the same approach described in 3DGS. Each primitive thus also stores a set of 48 SH coefficients, which aim to capture complex reflectance properties under varying angles of illumination and view. Because each coefficient is stored as a float, this set of SH parameters accounts for the majority of the memory used per primitive-by a significant margin compared to the geometric parameters. Thus, reducing memory consumption, in practice, hinges largely on either lowering the SH degree or decreasing the total number of primitives in the scene.

# 3.2 Rendering Process

We use a two-stage rendering process, beginning with per-primitive preprocessing and followed by per-pixel rasterization. This approach enables efficient parallelization by allowing many primitives to be processed in parallel before the final compositing stage.

Preprocessing. During preprocessing, we construct each primitive from the aforementioned features (i.e. the position, distances, and rotation). Given the camera pose, we then transform the primitives into the camera's coordinate system and calculate the view-dependent color based on the viewing direction. Afterwards, we project these primitives into the 3D affine ray space approximation introduced in EWA Splatting [Zwicker et al. 2001, 2002]. Because small primitives are needed to achieve high-fidelity reconstructions, and because the approximation error grows with increasing distance from the center points, we found that the resulting error remains negligible while still reducing overall performance overhead. Lastly, we compute each primitive's projected bounding box in screen space to later derive the pixels from which it is visible.

Global Sorting and Tiling. Following preprocessing, we leverage the tiling and global sorting techniques from 3DGS to map primitives to their corresponding pixels efficiently. We tile the screen into regions and sort primitives within each tile according to approximate front-to-back order.

Rasterization. During rasterization, each pixel ray either intersects a given primitive twice or not at all since the introduced primitives are convex. To find intersections, we use the Möller-Trumbore intersection algorithm (MTIA) [Möller and Trumbore 2005], which is fully differentiable and thus usable in our gradient-based optimization. If there are no intersections, the primitive is not visible; if there are two, the opacity depends on the distance between the intersection points. As our reconstruction is scale ambiguous, we must normalize the obtained intersection distances to ensure consistent appearance across different scene sizes. We do this by determining the smallest distance d of the primitives and then scaling all distance measurements accordingly in a manner similar to EVER [Mai et al. 2024]. *I.e.* given the opacity of a primitive  $\alpha$ , we define the density

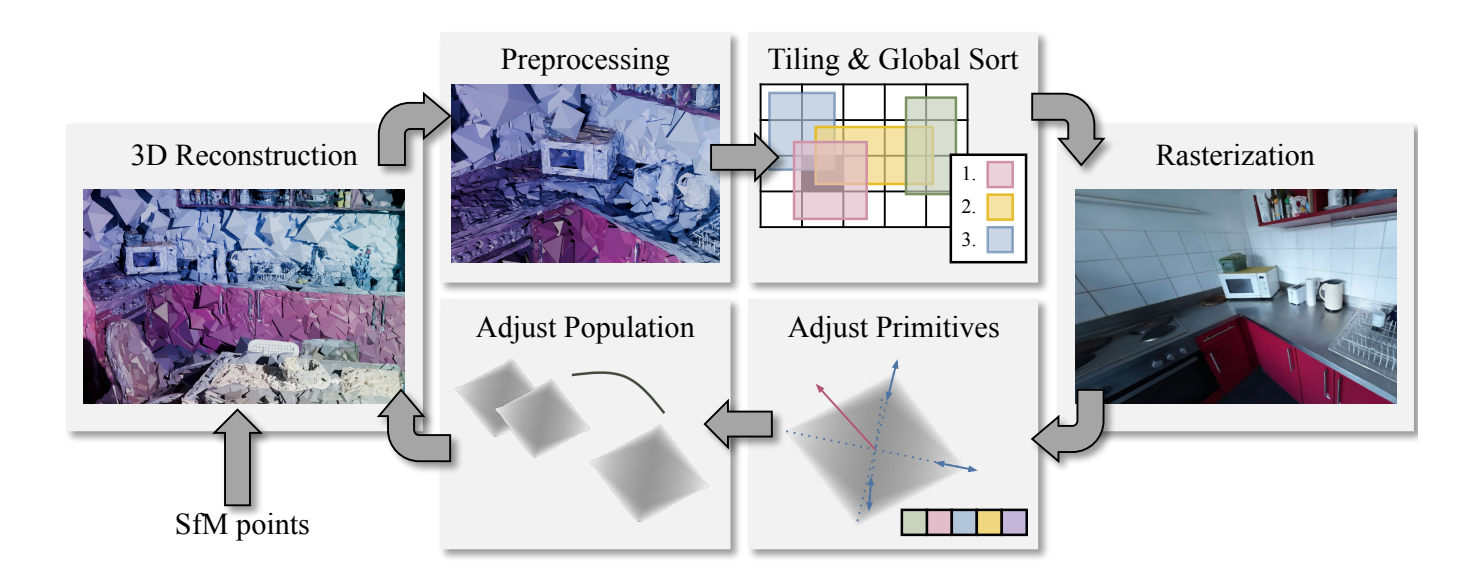


Fig. 3. **Overview** of our method. First, primitives are constructed from SfM points. During the rendering process, primitives are preprocessed to adjust them based on the camera pose. Afterward, a front-to-back sorted list of primitives for each tile is created. Lastly, during rasterization, the list is traversed to determine the pixel colors. By comparing the output to a known view, the primitives can then be adjusted using gradient descent. The gradients are similarly used to adjust the population of primitives dynamically.

of an octahedron as:

$$\sigma(\alpha) = -\frac{\log(1 - 0.99 \cdot \alpha)}{2 \cdot \min(d_x, d_y, d_z)}.$$
 (1)

Given the density and the two intersection depths  $i_1$ ,  $i_2$ , the opacity of an intersected primitive at a given pixel then follows as

$$o(i_1, i_2) = 1 - \exp(-\sigma(\alpha) \cdot (i_2 - i_1)).$$
 (2)

Compositing. Finally, we aggregate the color contributions of all visible primitives via alpha blending in front-to-back order. Because we maintain a sorted list of primitives for each tile, we can stop blending once cumulative opacity reaches a predefined threshold (i.e. 0.999), improving performance without noticeably affecting quality. While this approach simplifies behavior when primitives overlap, the end result is a high-fidelity rendering that faithfully reproduces fine geometry while being efficient enough for real-time applications.

#### 3.3 Anti-Aliasing

In the context of Gaussian kernels, Mip-Splatting [Yu et al. 2024] introduced two antialiasing methods for Gaussian primitives: a 3D smoothing filter and a 2D Mip filter. In conjunction, they are able to control the maximum frequency of primitives, mitigating aliasing and dilation artifacts.

We adopt their 3D smoothing strategy to limit how small primitives can become based on visibility from the training views. As a result, each primitive is visible from at least one pixel of a training view. However, applying their 2D Mip filter approach is not possible for our primitives because they rely on modifying the screen

space Gaussian distribution. Instead, for each primitive, we identify vertices that lie on the bounding box used for tiling and shift them outward, parallel to the screen. This effectively enlarges the bounding box footprint and increases the minimum size at which the primitive appears. Moreover, because the fall-off within each primitive is still treated as linear, expanding the distance from the center raises the opacity along the primitive as it is evaluated over a larger extent. Conceptually, this approach acts as a coarse approximation that serves to band-limit the high frequencies that would otherwise cause visible aliasing. Although this approach is not fully mathematically equivalent to a 2D Mip filter, it captures its function and empirically mirrors its behavior.

# 3.4 Optimization

We employ differentiable rendering to optimize our primitives' features from known views. For this, we use the loss formulation of 3DGS [Kerbl et al. 2023], consisting of L1 and SSIM terms:

$$\mathcal{L} = 0.8 \mathcal{L}_1 + 0.2 \mathcal{L}_{\text{D-SSIM}}.$$
 (3)

The gradients are then optimized using ADAM [Kingma and Ba 2017] and backpropagated through the entire rendering pipeline, effectively distributing the updates across the primitive features.

Rasterization Backpropagation. As a first step, backpropagation through the blending process yields gradients with respect to each primitive's alpha and color. When these gradients are propagated further, the alpha gradient indicates whether the primitive should be more or less transparent and, consequently, whether the intersections should move closer together or farther apart along the

pixel's ray. By following the resulting intersection gradients, we can adjust each primitive's center and vertices accordingly to achieve the desired changes. This corresponds to backpropagation through the MTIA, where the intersection depth is influenced by the position of each of the corners of the triangle. In turn, the positions of the corners depend on the position of the ray space center and the offsets to it. Combining the above, by aggregating over the corners and both intersections, we can propagate gradients from alpha to the geometric features.

Preprocessing Backpropagation. By this point, the gradients describe the loss w.r.t. the features that were originally passed to the rasterization step. While they already describe desired changes to the position of the center and corners, they do so in ray space. As a consequence, propagation through the preprocessing first involves reversing the projection and view transformations, yielding world space gradients. The final center gradients are a combination of the propagated ray space center gradients and the impact of the position on the ray space approximation and view-dependent color. Finally, the gradient flow w.r.t. to the corners splits when undoing the rotation, onto quaternion and distance features, respectively. As our scenes are scale ambiguous, we use the maximum distance between two training cameras to approximate their size and adjust the learning rates for position and distances accordingly.





Fig. 4. Visualization of our scene representation. We show all octahedra with an opacity of at least 0.25 on an optimized Mip-NeRF 360 [2022] Bicycle scene reconstruction.

# Population Control

While the above optimization process can effectively optimize a set of primitives, it cannot create or remove them if required. In addition to an initialization scheme, this raises the need for additional processes to control the population of primitives. While we generally adapt the processes introduced by 3DGS, they require adjustments to accommodate the novel primitives.

Initialization. We initialize a primitive for each Structure-from-Motion (SfM) [Schonberger and Frahm 2016] point using its position and color. Every primitive is constructed with equal distance features to all corners, using the distance between the corresponding SfM point and its closest neighbor as a starting point. While Gaussian kernels are circular when initialized and thus unaffected by rotations, our kernels are not. Thus, we initialize the primitives with a uniformly random rotation quaternion to create a more homogeneous spatial coverage.

Adaptive Population Control. Efficient population control requires processes to prune undesired primitives and create ones that can improve fidelity. For pruning, primitives are removed if they are too transparent, too large relative to the scene extent, or take up too much screen space of a known view. This necessitates defining the size of a primitive to determine these criteria. For octahedra, we define their size as their longest axis, i.e. twice the size of the longest distance. For tetrahedra, determining their largest possible depth is more involved, and we instead approximate using  $\sqrt{2}$  times the distance to the furthest corner.

Creating new primitives is realized as either cloning or splitting existing ones. For this, primitives that have large view-space positional gradients are chosen, with smaller ones being cloned and larger ones being split based on the size of the primitives, as described above, and the size of the scene. Cloning a primitive creates a new primitive with the same features but without the gradient momentum which is directly applicable to our representations.

Splitting, on the other hand, usually involves creating two new primitives with smaller sizes and placing them by sampling from the original Gaussian as a PDF. To adjust this for octahedra, since the distances are aligned with the coordinate axes and symmetric, we sample the new positions from a PDF with standard deviations set to the corresponding distance. This way, primitives are more likely to spread along the longer dimensions of the octahedra. For tetrahedra, this is not trivially possible and we instead set the standard deviations to a quarter of the largest distance for all dimensions.

A sample result of the resulting scene representation and population of octahedra can be seen in Figure 4.

#### 4 Experiments

We evaluate our results on Mip-NeRF 360 [Barron et al. 2022] and ScanNet++ v2 [Yeshwanth and Liu et al. 2023]. For Mip-NeRF 360, we use all 9 available scenes, while for ScanNet++, we use only the first five NVS scenes with available test views. We train and test on the official splits provided by each dataset and maintain consistent parameters across all evaluated scenes. All approaches are trained for 30k iterations.

Following prior work, we use Mip-NeRF 360 outdoor scenes at quarter resolution and indoor scenes at half resolution. For Scan-Net++ scenes, we use the official toolkit to undistort the images and use them at full resolution. All approaches are trained, rendered, and evaluated at the same resolution.

While there is a large body of work offering improvements to 3DGS, we mainly focus on the original work and the changes made by Mip-Splatting, as they most closely relate to the foundational changes made by our approach. We believe that much of the recent progress made on improving 3DGS can similarly be applied to our approach to further improve quality or performance metrics.

#### 4.1 Reconstruction Quality

We measure reconstruction quality using the standard image metrics PSNR, SSIM and LPIPS. On the ScanNet++ dataset, our method consistently achieves scores close to both 3DGS and Mip-Splatting despite using significantly fewer primitives, as visible in Table 1. We also compare against GS-MCMC [Kheradmand et al. 2024], which

	39f36da05b	5a269ba6fe	dc263dfbf0	08bbbdcc3d	fb564c935d	PSNR	SSIM	LPIPS	Primitives
3DGS [2023]	27.693	23.675	23.436	22.444	23.210	24.092	0.853	0.263	738k
Mip-Splatting [2024]	27.728	23.636	23.454	22.570	23.221	24.122	0.852	0.261	977k
GS-MCMC [2024]	27.902	23.787	23.782	23.657	23.371	24.500	0.862	0.256	255k
LinPrim (ours)	27.557	23.845	22.668	22.312	23.801	24.037	0.849	0.281	255k

Table 1. **Quantitative Results** on ScanNet++ v2 scenes [Yeshwanth and Liu et al. 2023]. We limit GS-MCMC [Kheradmand et al. 2024] to use as many primitives as our approach does on average. Our method generates results of comparable performance while using much fewer primitives than 3DGS [Kerbl et al. 2023] and Mip-Splatting [Yu et al. 2024].

	PSNR	SSIM	LPIPS	Primitives
Zip-NeRF [2023]	28.54	0.828	0.189	
Instant-NGP [2022]	25.68	0.705	0.302	
3DGS [2023]	27.43	0.813	0.217	3.32M
Mip-Splatting [2024]	27.79	0.827	0.203	4.17M
LinPrim (ours)	26.63	0.803	0.221	1.79M

Table 2. **Quantitative Results** on Mip-NeRF 360 scenes [Barron et al. 2022]. Our approach generates results comparable in performance while only using 54% of the primitives of 3DGS and 43% of Mip-Splatting.

allows precise limitations to the primitive population, and find that our results remain comparable, albeit slightly worse. For Mip-NeRF 360 scenes, we see a similar trend of comparable performance but with a more compact representation. Figures 6 and 7 illustrate that our method faithfully reconstructs many challenging regions while sometimes showing slightly lower overall fidelity. These outcomes stem, in part, from the bounded nature of our primitives, which enforce sharper, more "binary" decisions in underconstrained areas. In practice, this can lead to crisper reconstructions in reflective or transparent regions—such as glass or distant backgrounds—but can also result in more conspicuous edges on rarely observed surfaces like ceilings. Overall, we find our approach to work the best in smaller, more densely captured scenes, as it retains strong geometric and visual clarity without overly densifying frequently observed regions.

### 4.2 Tetrahedra Evaluation

In Table 3, we evaluate our tetrahedron approach using the same datasets, parameter constraints, and optimization framework described previously. By simply swapping octahedra for tetrahedra, we demonstrate that our method generalizes well to polyhedra with different geometric constraints and can still produce photorealistic reconstructions, as seen in Figure 5. Quantitatively, our tetrahedron approach performs similarly to octahedra on the ScanNet++ scenes and struggles on Mip-NeRF 360, highlighting the benefits of the increased symmetry and stability inherent to our octahedra.

Although our existing pipeline was designed primarily around octahedra, these results confirm that it is not narrowly tailored to one specific primitive type. Nonetheless, tetrahedra could likely benefit from specialized adaptive population control and projection techniques that fully consider their asymmetric geometry, potentially closing the performance gap on currently challenging scenes.



Fig. 5. **Qualitative Results** of our Tetrahedron approach on the Mip-NeRF 360 [2022] Bicycle scene and the ScanNet++ v2 [2023] 39f36da05b scene.

	S	canNet+	+	Mip-NeRF 360			
	PSNR	SSIM	LPIPS	PSNR	SSIM	LPIPS	
Octahedron	24.04	0.849	0.281	26.63	0.803	0.221	
Tetrahedron	24.05	0.848	0.302	25.96	0.790	0.247	

Table 3. **Comparison** of the performance of our Octahedron and Tetrahedron approaches on ScanNet++ v2 [2023] and Mip-NeRF 360 [2022] scenes. Both approaches produce comparable results on ScanNet++ scenes, but our Octahedron approach reaches higher reconstruction quality on Mip-NeRF 360 scenes.

For instance, tuning how we split tetrahedra could yield further gains in accuracy.

Notably, tetrahedra and octahedra both converge to similar final primitive counts. On average, we obtained 259k tetrahedra for Scan-Net++ scenes and 2.20M for Mip-NeRF 360, matching the counts of octahedra used in our experiments reasonably well. This suggests that switching between these primitive types does not inherently impose a significant memory or computational overhead. Future work on refining geometric constraints, feature parameterization, and splitting heuristics could unlock even better performance for tetrahedron-based approaches.

# 4.3 Rendering Speed

We evaluate the rendering speed of our methods by measuring the average time required to render every train and test view for each scene. All timings are recorded on a single RTX 3090 GPU at the same resolutions used for optimization, ensuring a fair comparison across all methods.

As shown in Table 4, all evaluated approaches achieve real-time performance, demonstrating that our primitives can be rendered interactively. Our octahedron-based method reaches 68fps on Scan-Net++ and 29fps on Mip-NeRF 360. Meanwhile, our tetrahedron variant achieves 175fps on ScanNet++ and 66fps on Mip-NeRF 360,

	ScanNet++	Mip-NeRF 360
3DGS [2023]	5.7ms	8.8ms
Mip-Splatting [2024]	11.0ms	20.3ms
Octahedron (ours)	14.6ms	34.6ms
Tetrahedron (ours)	5.7ms	15.2ms

Table 4. Quantitative Results on the rendering speed of tested approaches. We report the average time to render every train and test view on ScanNet++ v2 and Mip-NeRF 360 scenes.

making it about twice as fast as the octahedron approach due to having only half the faces to process per primitive.

These results confirm that the majority of the rendering cost stems from iterating over each face of each primitive to compute ray intersections. Since tetrahedra contain fewer faces, each pass requires less computational effort, thereby boosting the frame rate substantially. While our methods consistently demonstrate realtime rendering across both datasets, we must consider that the difference in primitive count can impact performance. Nevertheless, these experiments underscore the capability of our linear primitives, whether octahedra or tetrahedra, to balance high-fidelity reconstruction with the interactivity needed for real-time applications.

# Anti-Aliasing Ablation

Table 5 presents the effect of our antialiasing filters on reconstruction quality for one Mip-NeRF 360 and one ScanNet++ scene. We observe that enabling each filter individually improves quantitative performance, most prominently in PSNR. Combining both filters yields an even larger gain, indicating their complementary nature. Interestingly, LPIPS shows virtually no changes, suggesting that while our filters enhance pixel-level similarity, high-level perceptual features remain relatively stable. Neither filter significantly affects the number of primitives used in the reconstruction process, which indicates that these techniques refine visual fidelity without complicating the underlying geometry or increasing memory overhead. Overall, our results demonstrate that applying these filters leads to visually cleaner outputs and higher numerical scores, reinforcing the value of antialiasing.

Filt	ers	Bonsai			d	lc263dfbf0		
2D	3D	PSNR	SSIM	LPIPS	PSNR	SSIM	LPIPS	
		30.84	0.929	0.196	22.46	0.870	0.267	
$\checkmark$		30.96	0.931	0.196	22.59	0.870	0.266	
	$\checkmark$	30.97	0.930	0.195	22.66	0.871	0.266	
✓	$\checkmark$	31.21	0.936	0.195	22.67	0.871	0.266	

Table 5. Ablation showing the impact of the two filters used in our antialiasing efforts. Combining both filters reduces the reconstruction error.

#### 45 Limitations

While our method demonstrates comparable results and is easily understood and modified, it is not without drawbacks. First, the bounded nature of our primitives can introduce hard edges in poorly observed regions, resulting in more "segment-like" artifacts under limited view coverage. In these regions, the ability of Gaussian kernels to smoothly transition into each other leads to more visually pleasing results, even if the reconstruction is not necessarily better.

Second, the current population control processes are not as consistent as their Gaussian counterparts. While we did adapt the processes to our primitives, the underlying paradigms are not as suitable for our polyhedron primitives. More specifically, polyhedra could benefit from more specialized processes for placing newly split primitives and improved criteria for determining which areas should be densified. It would be especially interesting to explore enhancements to 3DGS that address the above issues, as such improvements could disproportionately benefit our polyhedron-based approaches.

#### Conclusion

We have presented novel approaches to volumetric scene reconstruction that leverage linear primitives, specifically octahedra and tetrahedra. Our method relies on a compact set of shape parameters and optimizes both geometry and appearance in a fully differentiable manner. By leveraging the inherent symmetries of octahedra, we achieve stable, high-fidelity results while maintaining a low memory footprint. At the same time, our experiments with tetrahedra demonstrate that the approach generalizes to other triangle-based volumes, underscoring its flexibility. Despite employing fewer primitives, our method consistently achieves comparable performance across challenging datasets, confirming its viability for real-world applications. Additionally, the bounded nature of our primitives yields more pronounced structural decisions in some rarely observed regions, sometimes leading to crisper reconstructions.

Promising future work could focus on leveraging the inherent properties of our representation. As a concrete example, while the rendering improvements made by EVER [Mai et al. 2024] create a lot of computational overhead for Gaussian-based approaches, the core requirements - discrete bounds and homogeneous density are already fulfilled by our primitives. A different avenue would be the incorporation of improved population control mechanisms. To summarize, we hope our linear primitives open up new possibilities for representing scenes in NVS applications and foster the creation of novel scene representations. Ultimately, the versatility of our approach presents a promising opportunity for representations that bridge the gap between NVS and the real world.

# References

Jonathan T. Barron, Ben Mildenhall, Matthew Tancik, Peter Hedman, Ricardo Martin-Brualla, and Pratul P. Srinivasan. 2021. Mip-nerf: A multiscale representation for anti-aliasing neural radiance fields. In Proceedings of the IEEE/CVF international conference on computer vision. 5855-5864. http://openaccess.thecvf.com/content/ ICCV2021/html/Barron\_Mip-NeRF\_A\_Multiscale\_Representation\_for\_Anti-Aliasing\_Neural\_Radiance\_Fields\_ICCV\_2021\_paper.html

Jonathan T. Barron, Ben Mildenhall, Dor Verbin, Pratul P. Srinivasan, and Peter Hedman. 2022. Mip-nerf 360: Unbounded anti-aliased neural radiance fields. In Proceedings of the IEEE/CVF conference on computer vision and pattern recognition. 5470-5479. http://openaccess.thecvf.com/content/CVPR2022/html/Barron\_Mip-NeRF\_ 360\_Unbounded\_Anti-Aliased\_Neural\_Radiance\_Fields\_CVPR\_2022\_paper.html

Jonathan T. Barron, Ben Mildenhall, Dor Verbin, Pratul P. Srinivasan, and Peter Hedman. 2023. Zip-NeRF: Anti-Aliased Grid-Based Neural Radiance Fields. https://doi.org/ 10.48550/arXiv.2304.06706 arXiv:2304.06706.

Haodong Chen, Runnan Chen, Qiang Qu, Zhaoqing Wang, Tongliang Liu, Xiaoming Chen, and Yuk Ying Chung. 2024a. Beyond Gaussians: Fast and High-Fidelity 3D Splatting with Linear Kernels. http://arxiv.org/abs/2411.12440 arXiv:2411.12440.

- Yiwen Chen, Zilong Chen, Chi Zhang, Feng Wang, Xiaofeng Yang, Yikai Wang, Zhongang Cai, Lei Yang, Huaping Liu, and Guosheng Lin. 2024b. GaussianEditor: Swift and Controllable 3D Editing with Gaussian Splatting. 21476–21485. https://openaccess.thecvf.com/content/CVPR2024/html/Chen\_GaussianEditor\_Swift\_and\_Controllable\_3D\_Editing\_with\_Gaussian\_Splatting\_CVPR\_2024\_paper.html
- Markus Gross and Hanspeter Pfister. 2011. Point-based graphics. Elsevier. https://books.google.com/books?hl=en&lr=&id=9LCQ86u9Sc4C&oi=fnd&pg=PP1&dq=point-based+graphics&ots=c3w0b2Lqmg&sig=p52E4HOjjWJa7m3EKfJu8F5HEhI
- Jan Held, Renaud Vandeghen, Abdullah Hamdi, Adrien Deliege, Anthony Cioppa, Silvio Giancola, Andrea Vedaldi, Bernard Ghanem, and Marc Van Droogenbroeck. 2024. 3D Convex Splatting: Radiance Field Rendering with 3D Smooth Convexes. https://doi.org/10.48550/arXiv.2411.14974 arXiv:2411.14974.
- Binbin Huang, Zehao Yu, Anpei Chen, Andreas Geiger, and Shenghua Gao. 2024. 2D Gaussian Splatting for Geometrically Accurate Radiance Fields. In Special Interest Group on Computer Graphics and Interactive Techniques Conference Conference Papers '24. ACM, Denver CO USA, 1–11. https://doi.org/10.1145/3641519.3657428
- Bernhard Kerbl, Georgios Kopanas, Thomas Leimkühler, and George Drettakis. 2023. 3D Gaussian Splatting for Real-Time Radiance Field Rendering. https://doi.org/10.48550/arXiv.2308.04079 arXiv.2308.04079.
- Shakiba Kheradmand, Daniel Rebain, Gopal Sharma, Weiwei Sun, Jeff Tseng, Hossam Isack, Abhishek Kar, Andrea Tagliasacchi, and Kwang Moo Yi. 2024. 3D Gaussian Splatting as Markov Chain Monte Carlo. http://arxiv.org/abs/2404.09591 arXiv:2404.09591.
- Diederik P. Kingma and Jimmy Ba. 2017. Adam: A Method for Stochastic Optimization. http://arxiv.org/abs/1412.6980 arXiv:1412.6980.
- Georgios Kopanas, Julien Philip, Thomas Leimkühler, and George Drettakis. 2021. Point-Based Neural Rendering with Per-View Optimization. Computer Graphics Forum 40, 4 (July 2021), 29–43. https://doi.org/10.1111/cgf.14339
- Alexander Mai, Peter Hedman, George Kopanas, Dor Verbin, David Futschik, Qiangeng Xu, Falko Kuester, Jonathan T. Barron, and Yinda Zhang. 2024. EVER: Exact Volumetric Ellipsoid Rendering for Real-time View Synthesis. https://doi.org/10.48550/arXiv.2410.01804 arXiv:2410.01804.
- Ben Mildenhall, Pratul P. Srinivasan, Matthew Tancik, Jonathan T. Barron, Ravi Ramamoorthi, and Ren Ng. 2022. NeRF: representing scenes as neural radiance fields for view synthesis. Commun. ACM 65, 1 (Jan. 2022), 99–106. https://doi.org/10.1145/3503250
- Tomas Möller and Ben Trumbore. 2005. Fast, minimum storage ray/triangle intersection. In *ACM SIGGRAPH 2005 Courses (SIGGRAPH '05)*. Association for Computing Machinery, New York, NY, USA, 7–es. https://doi.org/10.1145/1198555.1198746
- Thomas Müller, Alex Evans, Christoph Schied, and Alexander Keller. 2022. Instant neural graphics primitives with a multiresolution hash encoding. *ACM Transactions on Graphics* 41, 4 (July 2022), 1–15. https://doi.org/10.1145/3528223.3530127
- Johannes L. Schonberger and Jan-Michael Frahm. 2016. Structure-from-motion revisited. In Proceedings of the IEEE conference on computer vision and pattern recognition. 4104–4113. https://www.cv-foundation.org/openaccess/content\_cvpr\_2016/html/ Schonberger\_Structure-From-Motion\_Revisited\_CVPR\_2016\_paper.html
- Jiaxiang Tang, Jiawei Ren, Hang Zhou, Ziwei Liu, and Gang Zeng. 2024. DreamGaussian: Generative Gaussian Splatting for Efficient 3D Content Creation. https://doi.org/ 10.48550/arXiv.2309.16653 arXiv:2309.16653.
- Jiaxiang Tang, Hang Zhou, Xiaokang Chen, Tianshu Hu, Errui Ding, Jingdong Wang, and Gang Zeng. 2023. Delicate Textured Mesh Recovery from NeRF via Adaptive Surface Refinement. https://doi.org/10.48550/arXiv.2303.02091 arXiv:2303.02091 [cs].
- Peng Wang, Lingjie Liu, Yuan Liu, Christian Theobalt, Taku Komura, and Wenping Wang. 2023. NeuS: Learning Neural Implicit Surfaces by Volume Rendering for Multiview Reconstruction. https://doi.org/10.48550/arXiv.2106.10689 arXiv:2106.10689 [cs].
- Qiangeng Xu, Zexiang Xu, Julien Philip, Sai Bi, Zhixin Shu, Kalyan Sunkavalli, and Ulrich Neumann. 2022. Point-nerf: Point-based neural radiance fields. In Proceedings of the IEEE/CVF conference on computer vision and pattern recognition. 5438–5448. http://openaccess.thecvf.com/content/CVPR2022/html/Xu\_Point-NeRF\_Point-Based\_Neural\_Radiance\_Fields\_CVPR\_2022\_paper.html
- Yeshwanth and Liu, Matthias Nießner, and Angela Dai. 2023. Scannet++: A high-fidelity dataset of 3d indoor scenes. In *Proceedings of the IEEE/CVF International Conference on Computer Vision*. 12–22. http://openaccess.thecvf.com/content/ICCV2023/html/Yeshwanth\_ScanNet\_A\_High-Fidelity\_Dataset\_of\_3D\_Indoor\_Scenes\_ICCV\_2023\_paper.html
- Zehao Yu, Anpei Chen, Binbin Huang, Torsten Sattler, and Andreas Geiger. 2024. Mip-splatting: Alias-free 3d gaussian splatting. In Proceedings of the IEEE/CVF Conference on Computer Vision and Pattern Recognition. 19447–19456. https://openaccess.thecvf.com/content/CVPR2024/html/Yu\_Mip-Splatting\_Alias-free\_3D\_Gaussian\_Splatting\_CVPR\_2024\_paper.html
- Matthias Zwicker, Hanspeter Pfister, Jeroen Van Baar, and Markus Gross. 2001. EWA volume splatting. In *Proceedings Visualization*, 2001. VIS'01. IEEE, 29–538. https://ieeexplore.ieee.org/abstract/document/964490/

M. Zwicker, H. Pfister, J. van Baar, and M. Gross. 2002. EWA splatting. IEEE Transactions on Visualization and Computer Graphics 8, 3 (July 2002), 223–238. https://doi.org/ 10.1109/TVCG.2002.1021576 Conference Name: IEEE Transactions on Visualization and Computer Graphics.

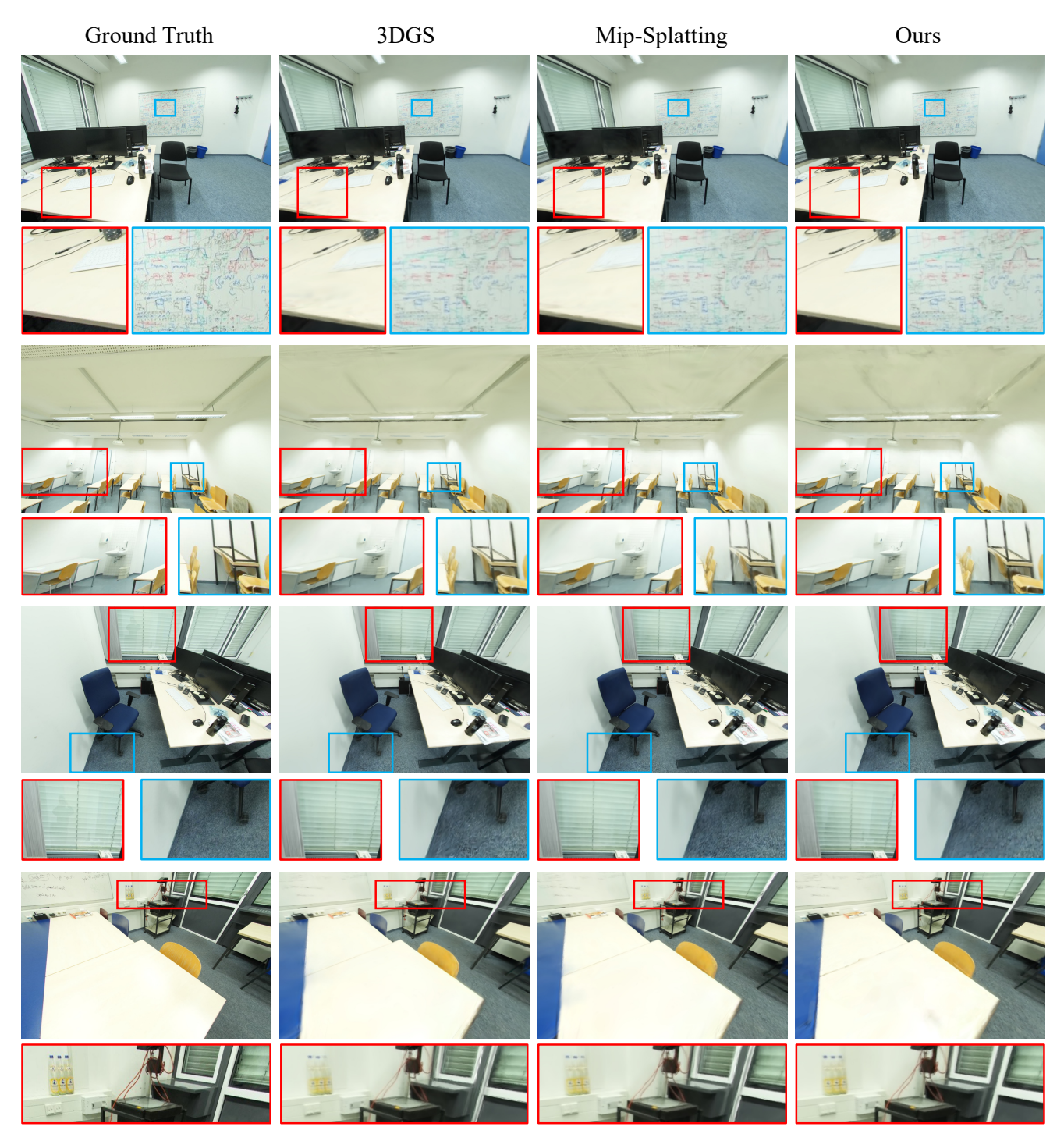


Fig. 6. **Qualitative Results** on test views from ScanNet++ v2 scenes [Yeshwanth and Liu et al. 2023].

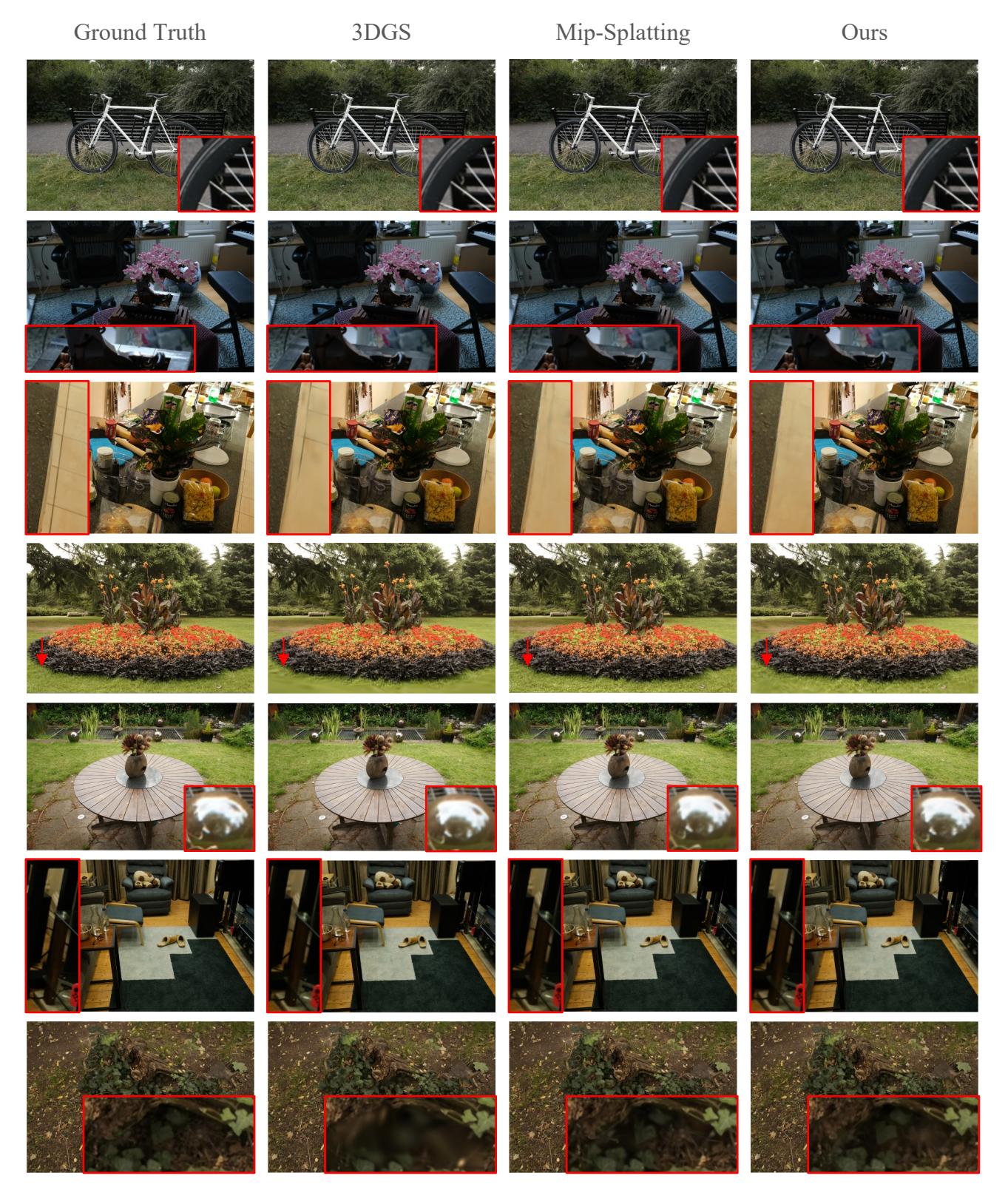


Fig. 7. Qualitative Results on test views from Mip-NeRF 360 scenes [Barron et al. 2022].